



3-D hybrid LES-RANS model for simulation of open-channel T-diversion flows

Jie ZHOU¹, Cheng ZENG*²

1. College of Environmental Science and Engineering, Hohai University, Nanjing 210098, P. R. China
2. Department of Civil and Structural Engineering, Hong Kong Polytechnic University, Hong Kong, P. R. China

Abstract: The study of flow diversions in open channels plays an important practical role in the design and management of open-channel networks for irrigation or drainage. To accurately predict the mean flow and turbulence characteristics of open-channel dividing flows, a hybrid LES-RANS model, which combines the large eddy simulation (LES) model with the Reynolds-averaged Navier-Stokes (RANS) model, is proposed in the present study. The unsteady RANS model was used to simulate the upstream and downstream regions of a main channel, as well as the downstream region of a branch channel. The LES model was used to simulate the channel diversion region, where turbulent flow characteristics are complicated. Isotropic velocity fluctuations were added at the inflow interface of the LES region to trigger the generation of resolved turbulence. A method based on the virtual body force is proposed to impose Reynolds-averaged velocity fields near the outlet of the LES region in order to take downstream flow effects computed by the RANS model into account and dissipate the excessive turbulent fluctuations. This hybrid approach saves computational effort and makes it easier to properly specify inlet and outlet boundary conditions. Comparison between computational results and experimental data indicates that this relatively new modeling approach can accurately predict open-channel T-diversion flows.

Key words: hybrid LES-RANS model; open-channel flow; T-diversion; turbulence modeling

1 Introduction

Open-channel dividing flows draw much attention in environmental and hydraulic engineering. They occur in many hydraulic structures of urban drainage systems and agricultural irrigation systems. Common types of diversion include T-diversions and Y-diversions. More studies have been devoted to T-diversions because they are more frequently used in irrigation and drainage systems and their flow structures are more complicated. Fig. 1 shows the typical flow pattern in a T-diversion. It contains a recirculation zone immediately downstream of the entrance of the branch channel, a contracted flow region in the branch channel, and a stagnation zone near the downstream corner of the diversion. In the region downstream of the main channel, separation due to flow expansion may occur with a high discharge ratio.

*Corresponding author (e-mail: c.zeng@live.com)
Received Aug. 6, 2009; accepted Sep. 8, 2009

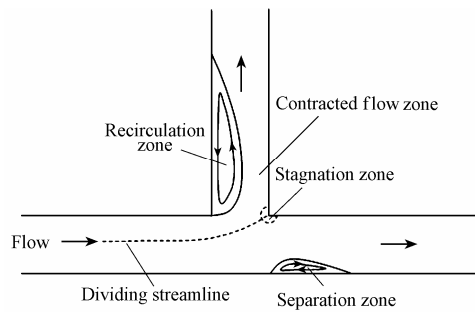


Fig. 1 Characteristics of open channel T-diversion flow

Numerical study of the flow in T-diversions is not easy because the flow is typically highly turbulent and three-dimensional. Several numerical simulations of the flow in open-channel T-diversions have been reported. Shettar and Murthy (1996) developed a two-dimensional numerical model that employed depth-averaged forms of the continuity and momentum equations together with $k-\varepsilon$ turbulence closure schemes to simulate the flow at open-channel T-divisions. Good agreement between their calculations and experimental measurements was reported for one test case with a discharge ratio of 0.52. To the authors' knowledge, the first three-dimensional turbulent flow simulation of T-diversion geometries was conducted by Issa and Oliveira (1994). They developed a numerical model that solves the fully three-dimensional two-fluid RANS equations for dispersed two-phase flow and the standard $k-\varepsilon$ equations for turbulence. Significant improvements in the predictions of stream velocity profiles at the symmetry plane in going from two-dimensional to three-dimensional simulations were reported. Neary et al. (1999) developed and validated a three-dimensional $k-\omega$ model for dividing flows in an open-channel T-diversion. Parametric study on the discharge ratios, aspect ratios and main channel-bed-roughness distribution was conducted. However, the lack of three-dimensional velocity measurements prohibited a more detailed assessment of the calculation. Ramamurthy et al. (2007) developed a three-dimensional $k-\omega$ model with free surface tracking capability to study open-channel dividing flows. For dividing flows in T-diversions, their model reproduces mean flow characteristics such as velocity profiles, water surface profiles and mean flow patterns. Recently, Li and Zeng (2009) developed a three-dimensional model with Spalart-Allmaras turbulence closure to investigate flows in channel diversions with varying width ratios and different vegetation densities in the branch channel. The numerical results quantitatively predict the trend of increasing flow in the branch channel with an increase in branch channel width and/or a decrease in vegetation density.

The present paper describes the formulation and application of a three-dimensional hybrid numerical model to simulate the flow in open-channel T-diversions. The unsteady RANS model is applied in the upstream and downstream regions of the main channel as well as the downstream region of the branch channel. The LES model is used in the channel diversion region. This hybrid model has two purposes: The first is to save computational effort,

as LES is computationally more intensive. The second is to relieve the limitations on the specification of the inlet and outlet boundary conditions solely for LES. Isotropic velocity fluctuations are added at the inflow interface of the LES region. Without the fluctuations, the resolved turbulence in the LES region will be too small and a long stream distance is required for the development of fully turbulent flow. At the outflow interface of the LES region, there are overlap regions of the computational domains of the LES and the RANS flow solver. The virtual body force is added inside this region. The goal is to drive the LES solution toward the mean velocity profiles of the RANS solution and dissipate the excessive turbulent fluctuations for the RANS computations.

2 Isotropic synthesized turbulence

A turbulent velocity field can be simulated using random Fourier modes. This method was proposed by Kraichnan (1970) and Karweit et al. (1991) and further developed by Bechara et al. (1994) and Bailly and Juvé (1999). Recently, Davidson and Billson (2006) evaluated the method of adding the isotropic synthesized turbulent fluctuations at the interface between the LES and RANS regions in order to trigger the equations to solve for turbulence. Fig. 2 shows the geometry of the n th Fourier mode in wave number space. The turbulence field is given by the following equation:

$$\begin{cases} u'(x, y, z) = 2 \sum_{n=1}^N \hat{u}^n \cos(\kappa_x^n x + \kappa_y^n y + \kappa_z^n z + \psi^n) \sigma_x^n \\ v'(x, y, z) = 2 \sum_{n=1}^N \hat{u}^n \cos(\kappa_x^n x + \kappa_y^n y + \kappa_z^n z + \psi^n) \sigma_y^n \\ w'(x, y, z) = 2 \sum_{n=1}^N \hat{u}^n \cos(\kappa_x^n x + \kappa_y^n y + \kappa_z^n z + \psi^n) \sigma_z^n \end{cases} \quad (1)$$

where \hat{u}^n and ψ^n are the amplitude and phase of the n th Fourier mode, respectively; κ_i^n ($i=x, y, z$) is the component of the wave number vector of the n th Fourier mode in the x , y , and z directions: $\kappa_x^n = |\boldsymbol{\kappa}^n| \sin \theta^n \cos \varphi^n$, $\kappa_y^n = |\boldsymbol{\kappa}^n| \sin \theta^n \sin \varphi^n$, and $\kappa_z^n = |\boldsymbol{\kappa}^n| \cos \theta^n$; σ_i^n ($i=x, y, z$) is the component of the unit vector of the n th Fourier mode in the x , y , and z directions: $\sigma_x^n = \cos \alpha^n \cos \theta^n \cos \varphi^n - \sin \alpha^n \sin \varphi^n$, $\sigma_y^n = \cos \alpha^n \cos \theta^n \sin \varphi^n + \sin \alpha^n \cos \varphi^n$, and $\sigma_z^n = \cos \alpha^n \sin \theta^n$; and N is the total number of Fourier modes, equal to 150 in the present simulation.

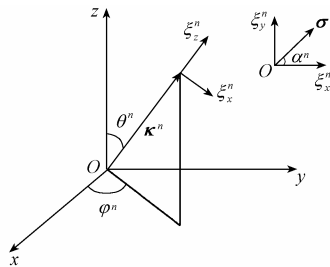


Fig. 2 Geometry for n th Fourier mode

The assumption of incompressibility of the continuity equation leads to the following condition:

$$\frac{\partial u'}{\partial x} + \frac{\partial v'}{\partial y} + \frac{\partial w'}{\partial z} = -2 \sum_{n=1}^N \hat{u}^n \sin(\kappa_x^n x + \kappa_y^n y + \kappa_z^n z + \psi^n) (\kappa_x^n \sigma_x^n + \kappa_y^n \sigma_y^n + \kappa_z^n \sigma_z^n) = 0 \quad (2)$$

Therefore,

$$\kappa_x^n \sigma_x^n + \kappa_y^n \sigma_y^n + \kappa_z^n \sigma_z^n = 0 \quad (3)$$

This means that the wave number vector $\boldsymbol{\kappa}^n$ and the velocity unit vector $\boldsymbol{\sigma}^n$ are orthogonal (in physical space) for each wave number. The direction of $\boldsymbol{\sigma}^n$ on the $\xi_x^n - \xi_y^n$ plane is randomly chosen through α^n . For each mode n , the random angles φ^n , α^n , and θ^n and the random phase ψ^n are generated through the specified probability distributions, which are given in Table 1.

Table 1 Probability distributions of random variables

Random variable	Probability	Range
φ^n	$1/2\pi$	$0 \leq \varphi^n \leq 2\pi$
α^n	$1/2\pi$	$0 \leq \alpha^n \leq 2\pi$
θ^n	$(\sin\theta)/2$	$0 \leq \theta^n \leq \pi$
ψ^n	$1/2\pi$	$0 \leq \psi^n \leq 2\pi$

The amplitude \hat{u}^n of each mode can be calculated with the following equation:

$$\hat{u}^n = \sqrt{E(|\boldsymbol{\kappa}^n|) \Delta |\boldsymbol{\kappa}^n|} \quad (4)$$

The turbulent kinetic energy $E(|\boldsymbol{\kappa}^n|)$ corresponds to the energy spectrum for isotropic turbulence. $\Delta |\boldsymbol{\kappa}^n|$ is a small interval in the spectrum at $|\boldsymbol{\kappa}^n|$. The spectrum is linearly divided into 150 intervals. A model spectrum is used to simulate the shape of an energy spectrum for isotropic turbulence. In this way, the sum of the squares of \hat{u}^n for all the Fourier modes is equal to the total kinetic energy of turbulence.

The chosen energy spectrum for isotropic turbulence is obtained experimentally, and defined as follows:

$$E(|\boldsymbol{\kappa}^n|) = \frac{2}{\pi} u'^2 \frac{\lambda}{1 + |\boldsymbol{\kappa}^n|^2 \lambda^2} \quad (5)$$

where u'^2 is the squared turbulence fluctuation of velocity in the x direction, and λ is the macro-scale of turbulence in open-channel flows. In free surface channel flow, λ is described by Nezu et al. (1994) as follows:

$$\begin{cases} \frac{\lambda}{h} = \sqrt{\frac{z}{h}} & \text{for } \frac{z}{h} < 0.6 \\ \frac{\lambda}{h} = 0.77 & \text{for } \frac{z}{h} \geq 0.6 \end{cases} \quad (6)$$

where h is the water depth, and z is the vertical ordinate measured from the bottom.

3 Outflow boundary treatment

The remaining flux from the downstream RANS computations to the upstream LES

computations can be significant because the LES computations are sensitive to the outflow conditions. For open-channel flows, the outflow conditions are determined by the so-called convective outflow condition, which is as follows:

$$\frac{\partial \phi}{\partial t} + u_c \frac{\partial \phi}{\partial n'} = 0 \quad (7)$$

where ϕ may be any scalar or velocity component, u_c is the convective velocity, and n' is the direction of the outward normal at the boundary.

In the present simulation, the outflow treatment for LES reported by Schlüter et al. (2005) is implemented at the interface between the LES region and the RANS region. This method is based on the body force, which is given by the following equation:

$$F_i(x) = \alpha \left(\langle \bar{u}_i \rangle_{\text{RANS}}(x) - \langle \bar{u}_i \rangle_{\text{LES}}(x) \right) \quad (8)$$

where $\langle \bar{u}_i \rangle_{\text{RANS}}(x)$ is the component of target velocities obtained from the RANS computation, and $\langle \bar{u}_i \rangle_{\text{LES}}(x)$ is the component of the time-averaged velocities obtained from the LES computation. The factor α can be determined by the strength of the body force. The forcing term involves only mean velocities, while the corresponding momentum equation is solved for the instantaneous velocities. By adding the forcing term to the momentum equation, the mean velocities from the LES computation are corrected without attenuating the resolved turbulent fluctuations. To achieve this goal, the averaging time for $\langle \bar{u}_i \rangle_{\text{LES}}(x)$ should be longer than the characteristic times of the turbulence. Eq. (8) also indicates that the forcing term needs to be zero if the actual mean velocity from the LES approaches the target velocity, which is a consistency requirement. Note that the RANS velocities are prescribed not only on one plane, but in the entire body force volume.

The estimate for an appropriate α can be determined from a one-dimensional analysis of the stationary Euler equations:

$$\frac{\partial u}{\partial t} + u \frac{\partial u}{\partial x} = -\frac{\partial p}{\partial x} + \alpha \left(\langle \bar{u} \rangle_{\text{RANS}} - \langle \bar{u} \rangle_{\text{LES}} \right) \quad (9)$$

where p is the pressure. Assuming a zero pressure gradient and a constant convection velocity with the bulk velocity u_B , the equation can be simplified. In addition, the flow is stationary, which means that $\langle \bar{u} \rangle_{\text{LES}} = u$. If $\langle \bar{u} \rangle_{\text{RANS}} = u_t$, Eq. (9) can be written as follows:

$$u_B \frac{\partial u}{\partial x} = \alpha (u_t - u) \quad (10)$$

This differential equation can be solved analytically and leads to the following expression:

$$u = u_t + (u_0 - u_t) \exp\left(-\frac{\alpha x}{u_B}\right) \quad (11)$$

where u_0 is the velocity at the beginning of the forcing region.

The value of α controls the characteristic response time of the LES to a change in the outlet boundary condition. The smaller the α is, the more ineffective the body force becomes, which may result in a drift of the outflow mean velocity profile toward the

unforced solution. Otherwise, a high value of α leads to a faster change in the desired velocity field, but may also lead to numerical instabilities. This method produced accurate results in the Schlüter et al. (2005) test case.

4 Turbulence model

4.1 Governing equation

The Navier-Stokes equation, averaged over time in the upstream and downstream regions of the main channel and filtered in the diversion region, is written as

$$\frac{\partial \bar{u}_i}{\partial t} + \frac{\partial (\bar{u}_i \bar{u}_j)}{\partial x_j} = -\frac{1}{\rho} \frac{\partial \bar{p}}{\partial x_i} + \frac{\partial}{\partial x_j} \left[(\nu_m + \nu_T) \frac{\partial \bar{u}_i}{\partial x_j} \right] + g_i \quad (i = 1, 2, 3) \quad (12)$$

$$\frac{\partial \bar{u}_i}{\partial x_i} = 0 \quad (i = 1, 2, 3) \quad (13)$$

where u_1 , u_2 , and u_3 (u , v , and w) are the velocity components in the x_1 , x_2 , and x_3 (x , y , and z ; or stream-wise, transverse, and vertical) directions; g_i is the gravitational acceleration component; ρ is the fluid density; ν_m is the molecular viscosity; and ν_T is the eddy viscosity: $\nu_T = \nu_t$ in the RANS regions, and $\nu_T = \nu_{SGS}$, the sub-grid scale viscosity, in the LES region.

The bar over the velocity components and pressure in Eqs. (11) and (12) indicates an average over time in the RANS region and filtering, or an average of the volume in the LES region. Thus, the flow variables are defined differently in the RANS region and the LES region. This may lead to an inconsistency at the interface between the RANS region and in the LES region. However, consistency is retained if we consider the RANS a very large eddy simulation (VLES) in which the flow variables are filtered using a large filtering length scale (equivalent to the RANS-defined turbulent length scale). In other words, the filtering is employed in both the RANS and LES regions, but with different length scales. The sub-grid length scale is determined by the distance from the closest surface in the RANS region, and by the cell size in the LES region.

4.2 Hybrid LES-RANS model

In this study, the eddy viscosity ν_T is specified by the Spalart-Allmaras turbulence model in the RANS region and the Smagorinsky model in the LES region. The Spalart-Allmaras turbulence model is formulated as follows:

$$\frac{\partial \nu}{\partial t} + u_j \frac{\partial \nu}{\partial x_j} = c_{b1} \tilde{S}_\nu \nu + \frac{1}{\sigma} \left\{ \frac{\partial}{\partial x_k} \left[(\nu + \nu_m) \left(\frac{\partial \nu}{\partial x_k} \right) \right] + c_{b2} \left(\frac{\partial \nu}{\partial x_k} \frac{\partial \nu}{\partial x_k} \right) \right\} - c_{w1} f_w \left(\frac{\nu}{d} \right)^2 + S_F \quad (14)$$

$$\nu_t = \nu f_{v1} \quad (15)$$

where ν is the working variable; S_F is the source term; d is the length scale;

$$\tilde{S}_v = S_v + \frac{\nu}{\kappa^2 d^2} f_{v2} \quad ; \quad S_v = \sqrt{\omega_j \omega_j} \quad ; \quad f_{v1} = \frac{\chi^3}{\chi^3 + c_{v1}^3} \quad ; \quad f_{v2} = 1 - \frac{\chi}{1 + \chi f_{v1}} \quad ; \quad \chi = \frac{\nu}{\nu_m} \quad ;$$

$$f_w = g \left(\frac{1 + c_{w3}^6}{g^6 + c_{w3}^6} \right)^{\frac{1}{6}} \quad ; \quad g = r + c_{w2} (r^6 - r) \quad ; \quad r = \frac{\nu}{\tilde{S}_v \kappa^2 d^2} \quad ; \quad c_{w1} = \frac{c_{b1}}{\kappa^2} + \frac{1 + c_{b2}}{\sigma} \quad ; \quad c_{w2} = 0.3 \quad ;$$

$$c_{w3} = 2 \quad ; \quad \kappa = 0.41 \quad ; \quad \sigma = \frac{2}{3} \quad ; \quad c_{b1} = 0.1335 \quad ; \quad c_{b2} = 0.622 \quad ; \quad c_{v1} = 7.1 \quad ; \quad \text{and } \omega_j (j=1,2,3) \text{ is the}$$

component of the rotation tensor in the x , y , and z directions.

The Spalart-Allmaras model is a one-equation model that is simpler than the commonly used $k-\varepsilon$ or $k-\omega$ model. It has been successfully applied in the modeling of certain free-shear flow, wall-bound flow and separated flow problems (Spalart and Allmaras 1994).

The Smagrinisky model is expressed as

$$\nu_{SGS} = L^2 \sqrt{2S_{ij}S_{ij}} \quad (16)$$

where ν_{SGS} is the sub-grid eddy viscosity, L is the turbulence characteristic length and will be discussed in the following section, and S_{ij} is the strain rate of the large scale or resolved field, defined as

$$S_{ij} = \frac{1}{2} \left(\frac{\partial \bar{u}_i}{\partial x_j} + \frac{\partial \bar{u}_j}{\partial x_i} \right) \quad (17)$$

The differences in the equations of the LES and RANS regions are the forms of the turbulent viscosity and the turbulence length scale.

4.3 Turbulence length scale

As discussed in section 4.2, the sub-grid model involves a length scale L . Near the wall, the small scale eddies are represented by the Prandtl mixing length $L_1 = C_0 z$, where $C_0 = 0.42$ is the von Karman's constant. In the outer flow region, the sub-grid scale L has the form, $L_2 = C_s \Delta$, where $\Delta = (\Delta x \Delta y \Delta z)^{1/3}$; Δx , Δy , and Δz are the grid dimensions in the x , y , and z directions; and $C_s = 0.1$ is the Smagrinisky constant. To match the near-wall Prandtl mixing length with the length scale in the outer flow region, a matching function is required. The matching function is significant because an incorrect matching function in the buffer regions will either damp out too much large-scale motion or produce excessive sub-grid scale motion.

It has been shown that the van Driest damping function cannot produce satisfactory results because of its coarse resolution (Shi et al. 2001). In this study, Mason's function (Mason and Thomson 1992) was used in the LES region:

$$\frac{1}{L^\beta} = \frac{1}{L_1^\beta} + \frac{1}{L_2^\beta} \quad (18)$$

Fig. 3 shows the length scales of the following validation case with various values of β . It can be seen that, as β increases, the profile becomes sharper and approaches the sub-grid length scale L_2 . Mason's matching function with the power $\beta = 2.5$ is equivalent to the van

Driest damping function.

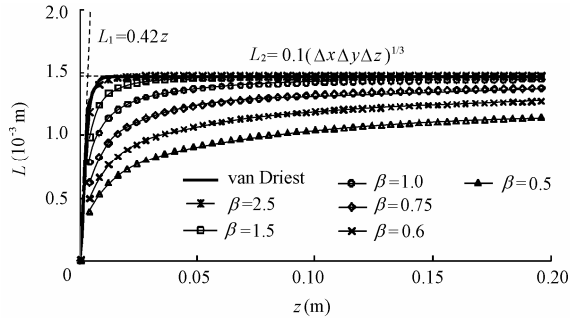


Fig. 3 Turbulence length scales for validation case

4.4 Computational methods and boundary conditions

In the method used in this study, Eqs. (12) and (13) are transformed by using the sigma-coordinate system to map the physical domain to a uniform transformed space in advance. Then, a split operator method is used to solve the transformed governing equations. In each time interval, Eq. (12) is split into three steps: advection, diffusion, and pressure propagation.

The QUICKEST scheme is used to solve the equations of pure advection. The scheme is third-order accurate and can eliminate second-order numerical diffusion. In the diffusion step and pressure propagation step, the central difference scheme is used in the space discretization. For continuity requirements, the pressure propagation equation should be substituted into the continuity equation to obtain the Poisson equation, which is solved with the conjugate gradient stabilized method. More details about the numerical method can be found in the research of Lin and Li (2002) and Li and Wang (2000).

Various types of boundary conditions are implemented in the model. These boundary conditions are applied at each split step. The free surface is an interface of water and air, at which both the dynamic and kinematic conditions should be satisfied. The dynamic condition can be satisfied by specifying zero pressure and zero gradients for all the velocity components if the surface tension and the wind stress on the free surface are ignored. Assuming no overturning occurs and the surface is relatively mild, the kinematic condition can be described as follows:

$$\frac{\partial \eta}{\partial t} = \bar{u}_3 - \bar{u}_1 \frac{\partial \eta}{\partial x_1} - \bar{u}_2 \frac{\partial \eta}{\partial x_2} \quad (19)$$

where η is the free surface elevation. The equation is an advection equation that can be solved by the QUICKEST scheme. Based on the no-slip boundary condition, flow velocities in all directions need to be zero at the bottom or at a solid wall. This treatment is accurate only when fairly fine grids are used to resolve the bottom boundary layer. Alternatively, the free-slip boundary condition can be used to calculate velocity gradients at the first interior node, and is subsequently used in the advection calculation. Meanwhile, the log-law wall function is used to calculate the wall shear stress that will be used in the diffusion step. The

latter method can produce accurate results with relatively coarse grids. At the inflow boundary, the gradient of the water surface elevation is assumed to be zero and the inflow rate with a predetermined velocity distribution is specified.

5 Validation

The three-dimensional hybrid LES-RANS model described above was validated with free surface open channel flow at $Re_\tau = u_\tau h / \nu_m = 2000$, where u_τ is the bed shear velocity. This flow corresponds to a bulk Reynolds number of 48 000, and is considered high enough for the assessment of the present model for practical applications. The major source of turbulence was from the bed shear stress at the bottom.

The dimensions of the channel section were $3.2 \text{ m} \times 1.6 \text{ m} \times 0.2 \text{ m}$. A coarse uniform mesh was chosen for this study. The mesh had 81 grid points in both the stream-wise (x) and the transverse (y) direction, and 51 grid points in the vertical (z) direction. This means that $\Delta x^+ (= u_\tau \Delta x / \nu_m)$, $\Delta y^+ (= u_\tau \Delta y / \nu_m)$, and $\Delta z^+ (= u_\tau \Delta z / \nu_m)$ were approximately 488, 244, and 48.8, respectively. The flow was sub-critical with a mean velocity of 0.24 m/s. The RANS model was applied in the upstream and downstream regions of the single channel and the LES model was used in the middle region. The upstream and downstream interfaces of the LES and the RANS regions were located at $x = 0.4 \text{ m}$ and $x = 2.8 \text{ m}$, respectively (Fig. 4). For Mason's function (Eq. (18)), the power $\beta = 0.5$ was chosen after several trial simulations due to its better performance. In the overlap region, the forcing constant was set to $\alpha = 10.0$.

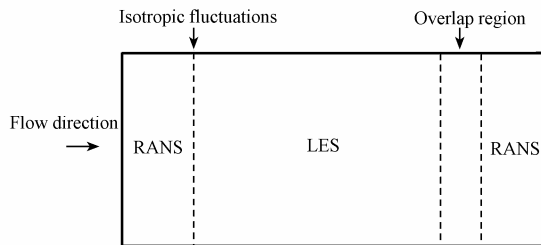


Fig. 4 LES and RANS regions (not to scale)

The purpose of this validation study was to assess the accuracy of the computed velocity components in the LES region. The RANS model was used to save computational effort and to facilitate the specification of stable inlet and outlet boundary conditions. Therefore, comparison of results was only performed for the velocities in the LES region. A typical field plot of the instantaneous velocity U , which was normalized by the maximum stream-wise velocity, is shown in Fig. 5. Fig. 6 shows the dimensionless mean stream-wise velocity u^+ ($u^+ = u / u_\tau$) versus z^+ , where z^+ is the dimensionless vertical distance from the bottom, which is defined as $z^+ = z u_\tau / \nu_m$. To quantitatively validate the calculation, the corresponding experimental data (Nezu et al. 1994) and direct numerical simulation (DNS) results (Hoyas and Jiménez 2006) are also plotted in Fig. 6. The calculated results are fairly good.

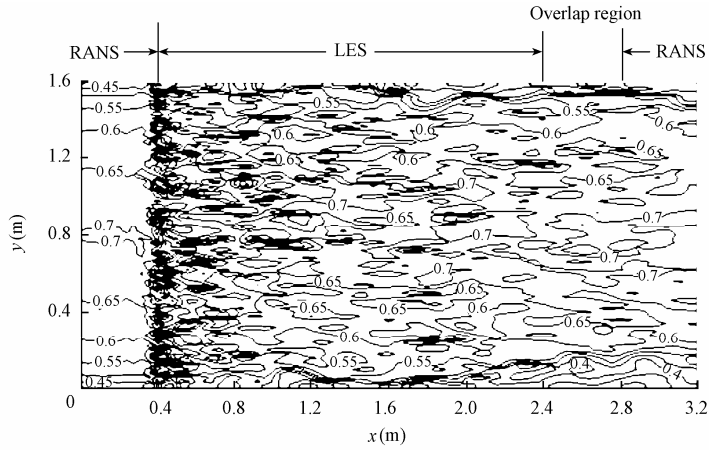


Fig. 5 Field plot of instantaneous velocity U

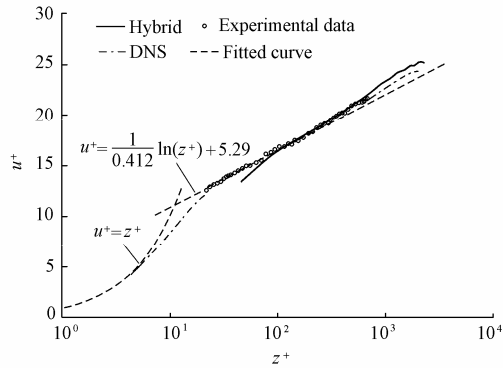


Fig. 6 Profile of mean stream-wise velocity in LES region

Fig. 7 shows the computed root mean square (RMS) velocities normalized by the shear velocity u_τ in the stream-wise, transverse, and vertical directions (u_{rms}^+ , v_{rms}^+ , and w_{rms}^+) and their comparison with the DNS results. It can be seen that the stream-wise RMS values show reasonable agreement with the DNS results. However, greater differences are evident between the transverse and vertical RMS values of the present simulation and the DNS, particularly near the wall.

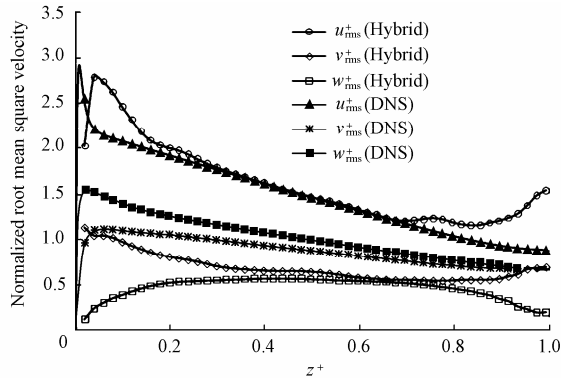


Fig. 7 Profile of root mean square velocity in LES region

6 Results and discussion

Detailed measurements of velocity and water surface profiles in open-channel T-diversion flows were carried out by Ramamurthy et al. (2007). The experimental setup consisted of a 6.198-m long main channel and a 2.794-m long branch channel. The main channel and the branch channel were 0.305 m high and 0.610 m wide, respectively. The branch channel was positioned at a distance of 2.794 m from the main channel entrance. The channel bed was horizontal everywhere. The upstream discharge Q_u was $0.046 \text{ m}^3/\text{s}$, and the discharge of the branch channel Q_b was $0.038 \text{ m}^3/\text{s}$. Hence, the discharge ratio Q_b/Q_u was 0.83.

The simulation using the hybrid model was conducted based on these experimental conditions. The computational domain and the interfaces of the LES and RANS regions, together with the overlap regions, were carefully chosen and are shown in Fig. 8. The width W of the channel was 0.610 m. Because the forcing fluctuations were added in the upper reach of the main channel, the length of the main channel upstream of the diversion was shortened to 2.44 m ($4W$). However, the lengths of the main channel downstream of the diversion and the branch channel were extended to 4.27 m ($7W$), since a large recirculation zone downstream may cause computational instability at the outlets. In the simulation, non-uniform grids were used in the RANS regions, and uniform grids were used in the LES region. The power $\beta = 1.0$ was used for Mason's matching function to determine the length scales in the LES region. The forcing constant α was set to 16.0 in the two overlap regions. In the physical experiments, the downstream water depth of the branch channel Y_b was not reported. The trial and error approach was thus used to specify Y_b in the numerical simulation such that the resulting discharge ratio equaled 0.83.

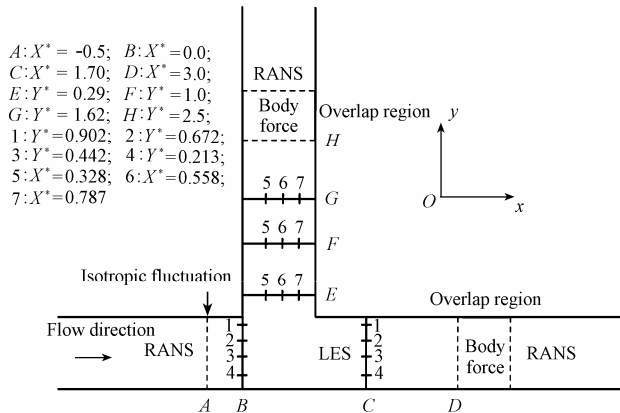


Fig. 8 Sketch of open-channel T-diversion flow

The time step was 0.002 s, and a dynamic steady state was achieved at around 50 s. The

mean statistics were collected from 50 s to 90 s. Fig. 9 shows the vector plots for the measured and predicted plane dimensionless mean velocity distribution at $Z^* = 0.27$ in the diversion region. In order to compare them with the experimental data, the original coordinates of the present simulation (x, y and z) have been transformed to X^*, Y^* and Z^* to coincide with the experiment. From these two plots, it can be seen clearly that there exist two separation zones in the diversion region that agree with the typical flow pattern previously reported. The computed flow pattern and the experimental data are in good agreement, although the results predict a slightly shorter reattachment length of the recirculation bubble in the branch channel.

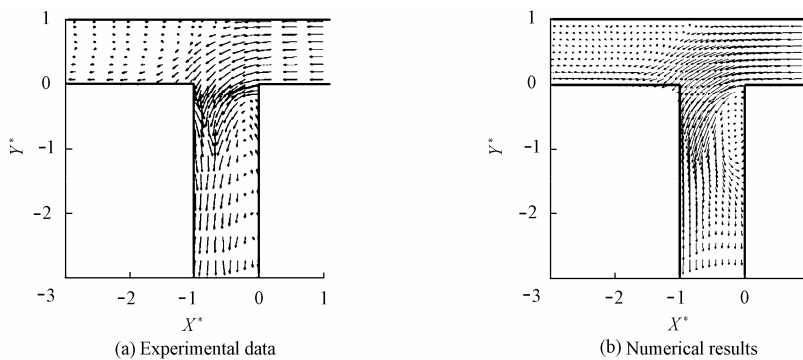


Fig. 9 Flow pattern of open-channel T-diversion flow at $Z^* = 0.27$

For detailed quantitative comparison, the computed mean velocity U^* ($U^* = -u/u_{\text{cri}}$, where u_{cri} is the critical velocity, and $u_{\text{cri}} = (gQ_u/W)^{1/3}$) in the main channel and V^* ($V^* = -v/u_{\text{cri}}$) in the branch channel at selected cross sections (shown in Fig. 8) are plotted in Fig. 10 and Fig. 11, together with the corresponding experimental data and the previous RANS results. The agreement between the computed mean velocity U^* and the measured velocities is excellent, and the agreement between the computed mean velocity V^* and the measured velocities is satisfactory. According to the comparison between the computed results and the previous RANS results, the predictive accuracy has been significantly improved in the branch channel, which means that the hybrid model is more suitable for the simulation of T-diversion flows. In the main channel, the positive values of U^* at locations C_3 and C_4 indicate the existence of the separation zone. In the branch channel, V^* is negative near the channel bottom and positive near the water surface at the locations E_5, F_5 and G_5 , which indicates that the recirculation zone is wider at the top. Verification of some turbulence statistics, such as the RMS values of the velocity components and the Reynolds shear stress, cannot be done due to lack of experimental data. This requires further study.

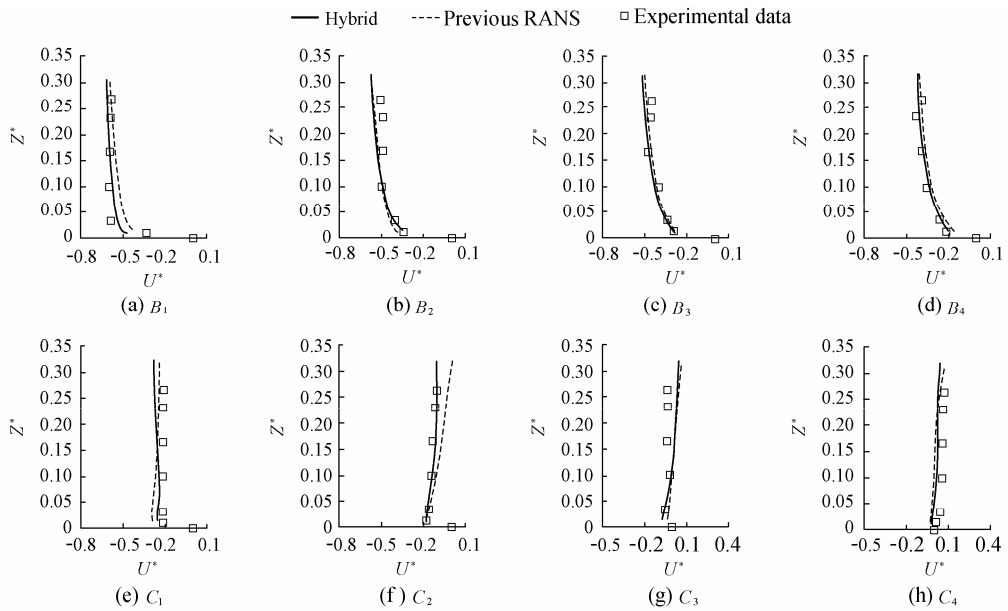


Fig. 10 Vertical variation of U^* in different sections of main channel

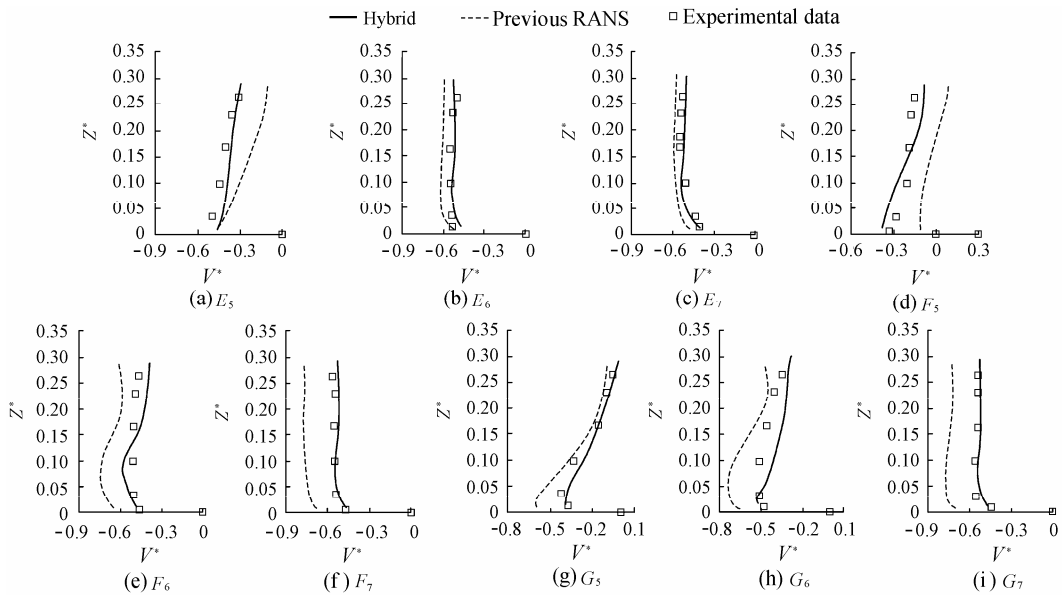


Fig. 11 Vertical variation of V^* in different sections of branch channel

7 Conclusions

A relatively new three-dimensional hybrid LES-RANS model has been developed to simulate open-channel T-diversion flows. The model was verified with a classical case of fully developed open-channel turbulent flow. The model was then used to simulate the flow in an open-channel T-diversion. Comparison between the numerical results and the detailed velocity

measurements shows that the hybrid model faithfully reproduces the mean flow characteristics, such as velocity profiles and mean flow patterns. With resolved turbulence, further work on the turbulent characteristics of T-diversion flows can be carried out.

References

- Bailly, C., and Juvé, D. 1999. A stochastic approach to compute subsonic noise using linearized Euler's equations. *Proceedings of the 5th AIAA/CEAS AeroAcoustics Conference and Exhibit*, 496-506. Seattle: American Institute of Aeronautics and Astronautics.
- Bechara, W., Bailly, C., Lafon, P., and Candel, S. M. 1994. Stochastic approach to noise modeling for free turbulent flows. *AIAA Journal*, 32(3), 455-463.
- Davidson, L., and Billson, M. 2006. Hybrid LES-RANS using synthesized turbulent fluctuations for forcing in the interface region. *International Journal of Heat and Fluid Flow*, 27(6), 1028-1042.
- Hoyas, S., and Jiménez, J. 2006. Scaling of the velocity fluctuations in turbulent channel up to $Re_\tau=2003$. *Physics of Fluids*, 18(1). [doi:10.1063/1.2162185]
- Issa, R. I., and Oliveira, P. J. 1994. Numerical prediction of phase separation in two-phase flow through T-junctions. *Computers Fluids*, 23(2), 347-372.
- Karweit, M., Blanc-Benon, P., Juvé, D., and Comte-Bellot, G. 1991. Simulation of the propagation of an acoustic wave through a turbulent velocity field: A study of phase variance. *Journal of the Acoustical Society of America*, 89(1), 52-62.
- Kraichnan, R. H. 1970. Diffusion by a random velocity field. *Physics of Fluids*, 13(1), 22-31. [doi:10.1063/1.1692799]
- Li, C. W., and Wang, J. H. 2000. Large eddy simulation of free surface shallow-water flow. *International Journal for Numerical Methods in Fluids*, 34(1), 31-46. [doi:10.1002/1097-0363(200915)34:1]
- Li, C. W., and Zeng, C. 2009. 3D numerical modeling of flow divisions at open channel junctions with or without vegetation. *Advances in Water Resources*, 32(1), 49-60. [doi:10.1016/j.advwatres.2008.09.005]
- Lin, P., and Li, C. W. 2002. A σ -coordinate three-dimensional numerical model for surface wave propagation. *International Journal for Numerical Methods in Fluids*, 38(11), 1045-1068. [doi:10.1002/flid.258]
- Mason, P. J., and Thomson, D. J. 1992. Stochastic backscatter in large-eddy simulations of boundary layers. *Journal of Fluid Mechanics*, 242, 51-78. [doi:10.1017/s0022112092002271]
- Neary, V. S., Sotiropoulos, F., and Odgaard, A. J. 1999. Three-dimensional numerical model of lateral-intake inflows. *Journal of Hydraulic Engineering*, 125(2), 126-140. [doi:10.1061/(ASCE)0733-9429(1999)125:2(126)]
- Nezu, I., Nakagawa, H., and Jirka, G. H. 1994. Turbulence in open-channel flows. *Journal of Hydraulic Engineering*, 120(10), 1235-1237. [doi:10.1061/(ASCE)0733-9429(1994)120:10(1235)]
- Ramamurthy, A. S., Qu, J., and Vo, D. 2007. Numerical and experimental study of dividing open-channel flows. *Journal of Hydraulic Engineering*, 133(10), 1135-1144. [doi:10.1061/(ASCE)0733-9429(2007)133:10(1135)]
- Schlüter, J. U., Pitsch, H., and Moin, P. 2005. Outflow conditions for integrated large eddy simulation/ Reynolds-averaged Navier- Stokes simulations. *AIAA Journal*, 43(1), 156-164.
- Shettar, A. S., and Murthy, K. K. 1996. A numerical study of division of flow in open channels. *Journal of Hydraulic Research*, 34(5), 651-675.
- Shi, J., Thomas, T. G., and Williams, J. J. R. 2001. Coarse resolution large-eddy simulation of turbulent channel flows. *International Journal of Numerical Methods for Heat and Fluid Flow*, 11(1), 20-35. [doi:10.1108 /09615530110364060]
- Spalart, P. R., and Allmaras, S. R. 1994. A one-equation turbulence model for aerodynamic flows. *La Recherche Aérospatiale*, 1, 5-21.